Progress In Electromagnetics Research, Vol. 174, 55–73, 2022

A Review of Multifunctional Optical Gap-Surface Plasmon Metasurfaces

Fei Ding*

Abstract—Gap-surface plasmon (GSP) metasurfaces that consist of metallic resonators, a middle dielectric spacer, and a back metallic reflector have become an emerging research area due to their excellent properties, such as ease of fabrication, high efficiency, and unprecedented capabilities of controlling reflected fields. In this concise review, we introduce our efforts in exploring the physical principles and fascinating applications of multifunctional GSP metasurfaces in the optical range. Starting with a typical GSP meta-atom, we present the concept and mechanism of simultaneous and independent phase and polarization control. We then overview some typical applications of GSP metasurfaces, including beam-steering, surface plasmon polariton coupling, metalenses, meta-waveplates, and dynamical metasurfaces. The review is ended with a short perspective on future developments in this area.

1. INTRODUCTION

The capability of manipulating light is tantalizingly attractive and promising for a wide range of applications. Conventional optics is governed by ray tracing within a material to gradually modulate the optical properties like phase, amplitude, and polarization, thereby resulting in bulky configurations and complex shapes. Therefore, the bulky nature of conventional optics limits modern technology to flexibly engineer and integrate the components for desired applications with compact footprints and multiple functionalities. The general solution is to design artificial structural units on the subwavelength scale with arbitrary optical responses to control the light-matter interaction with unprecedented capabilities, which can be flexibly achieved with metamaterials [1–6]. As metamaterials rely on complex three-dimensional (3D) unit cells, some practical issues, such as the high insertion losses and impractical accuracy requirement from nanofabrication, hinder the practical applications. To ease the complexities of metamaterials, their two-dimensional (2D) analog, known as metasurfaces, introduce reduced-dimensionality to simplify the constraints on material and geometric parameters while maintaining the ability to manipulate the optical waves [7–13]. Soon after, metasurfaces have attracted progressively increasing attention and become a flourishing research field. Generally, metasurfaces represent a promising and unique platform for versatile planar optics with judiciously designed meta-atoms [8–13]. Among all kinds of metasurfaces, gap-surface plasmon (GSP) metasurfaces, a particular branch that consists of metallic resonators, a middle spacer layer, and a bottom metallic reflector, have become an emerging research area due to their excellent properties, such as ease of fabrication, surface-confined configurations, high efficiency, and unprecedented capabilities of controlling reflected fields with subwavelength spatial resolutions. In this concise review, we introduce our efforts in multifunctional optical GSP metasurfaces. Starting with a typical GSP meta-atom, we present the concept and physical mechanism of simultaneous and independent control of phase and polarization. We then overview some typical applications of passive GSP metasurfaces including beam-steering, surface plasmon polariton

Received 3 February 2022, Accepted 17 May 2022, Scheduled 7 June 2022
* Corresponding author: Fei Ding (feid@mci.sdu.dk).
The author is with the SDU Nano Optics, University of Southern Denmark, Campusvej 55, DK-5230 Odense, Denmark.

(SPP) coupling, metalenses, and meta-waveplates. After that, we introduce our recent development in dynamical GSP metasurfaces. Finally, we summarize and provide a short perspective on the potential future direction in this area.

2. FUNDAMENTALS OF GSP META-ATOMS

We first present our design principle to realize multifunctional GSP metasurfaces for independent and complete control of phase and polarization with high refection efficiency and subwavelength spatial resolution. Figure 1(a) illustrates the schematic of a typical GSP meta-atom unit cell, which consists of a topmost cross-shaped gold (Au) nanoantenna, a middle silicon dioxide (SiO_2) dielectric spacer, and an optically thick bottom Au layer [14]. Upon excitation with a linearly polarized (LP) plane wave, denoted as TM- or TE-polarization with the electric field along the x- or y-axis (i.e., x- or y-polarization), SPPs are first excited on the metal-dielectric interfaces and then couple to each other because of the near-field effect, resulting in the GSP resonance with out-of-phase currents in the two metal strips and a maximum of the magnetic field in the gap [15, 16], which is also known as magnetic resonance [17, 18]. At the same time, the GSP mode is bouncing back and forth in the lateral direction and forms a standing wave due to the termination of the topmost Au nanoantenna. The resonance position is mainly determined by the length of the antennas and the effective mode index of GSP resonance [19–22]. As such, the optical responses can be independently tuned by varying the nano-cross dimensions L_x, L_y, and w, which stands for three degrees of freedom (DoFs) to control the reflected light with other parameters fixed, superior to brick-shaped meta-atoms with two DoFs [23, 24]. Here it should be mentioned that the near-field coupling becomes less pronounced and the GSP resonance gradually transits to a Fabry-Pérot resonance in the vertical direction when the spacer thickness is getting larger. In a more general scenario, this GSP meta-atom can be analytically explained by the coupled mode theory [25–27], where the radiative and intrinsic losses of the resonant mode can be identified and fully controlled by varying the geometrical/material parameters of the metal-insulator-metal (MIM) structure to control the reflected light, thereby leading to a complete phase diagram for researchers [27].

Considering the complex reflection coefficient under x-polarization in Figure 1(b), we find that the

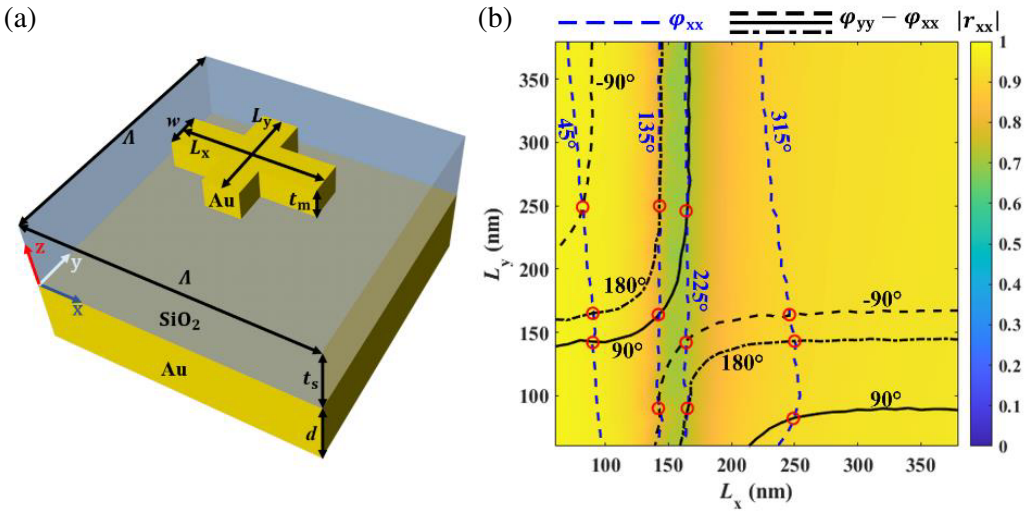

Figure 1. (a) Schematic of a typical GSP meta-atom unit cell consisting of across-shaped Au nanoantenna, a SiO_2 spacer, and a back Au reflector. (b) Simulated reflection amplitude $|r_{xx}|$ as a function of L_x and L_y for the meta-atom with other fixed dimensions of $\Lambda = 400\,\text{nm}$, $w = 50\,\text{nm}$, $t_m = 40\,\text{nm}$, and $t_s = d = 100\,\text{nm}$ at $\lambda = 850\,\text{nm}$ under x-polarization. The blue dashed lines represent the contours of the reflection phases φ_{xx} while black lines indicate the meta-QWPs and meta-HWPs with the phase difference $\Delta\varphi = \varphi_{yy} - \varphi_{xx}$ equal to $\pm 90°$ and $180°$. Reproduced from Ref. [14].

reflection phase φ_{xx} exhibits a fast variation near the GSP resonance while the reflection amplitude $|r_{xx}|$ remains at a high level with a proper spacer thickness [16, 27]. By spanning the while dimension space, the reflection phase φ_{xx} can nearly cover the 2π range, which is strongly dependent on L_x while L_y has a negligible effect. Due to the global symmetry along the x- and y-axis, the complex reflection coefficient for y-polarization can be easily obtained by mirroring the amplitude map and phase contours for x-polarization along the line $L_x = L_y$. Therefore, the reflection phase contour lines are almost parallel, causing all the x- and y-polarized contour lines to intersect each other, thereby enabling, independently and simultaneously, controlling the phase of reflected light in two linear polarizations [24]. Meanwhile, the cross-polarized reflection components, such as r_{yx} and r_{xy}, do not exist in the considered configuration. As a result, the optical response of such a GSP meta-atom can be described by the following diagonal Jones matrix in the linear polarization basis:

$$R_{LP} = \begin{pmatrix} r_{xx} & 0 \\ 0 & r_{yy} \end{pmatrix} \tag{1}$$

with $r_{xx} = |r_{xx}|e^{i\varphi_{xx}}$ and $r_{yy} = |r_{yy}|e^{i\varphi_{yy}}$ being the complex reflection coefficients for light polarized along two main axes of the meta-atom (i.e., x- and y-directions), which are mainly determined by the meta-atom dimensions. If the meta-atom is isotropic (i.e., $L_x = L_y$), r_{xx} andr_{yy} are identical, resulting in polarization-insensitive responses [28–30]. On other hand, distinct optical responses can be achieved with an anisotropic meta-atom under two orthogonal LP excitations. As such, linear-polarization-controlled meta-devices can be accordingly implemented with improved efficiency and decreased cross-talk [23, 24]. In addition, metasurface-based waveplates with versatile birefringence can be realized at any interested wavelength range. For example, metasurface-enabled half-waveplates (HWPs) and quarter-waveplates (QWPs) could be realized once the reflection amplitudes are equal ($|r_{xx}| = |r_{yy}|$) and the relative phase difference between two LP excitations, $\Delta\varphi = \varphi_{yy} - \varphi_{xx}$, is 180° [31–35] and ±90° [14, 34–37], respectively.

If the meta-atom in Figure 1(a) is rotated by an angle of θ counterclockwise with respect to the x-axis, the Jones matrix is modified as:

$$R_{LP}(\theta) = \begin{pmatrix} \cos\theta & -\sin\theta \\ \sin\theta & \cos\theta \end{pmatrix} \begin{pmatrix} r_{xx} & 0 \\ 0 & r_{yy} \end{pmatrix} \begin{pmatrix} \cos\theta & \sin\theta \\ -\sin\theta & \cos\theta \end{pmatrix} \tag{2}$$

For a normally incident CP beam with $E_{in} = \begin{pmatrix} 1 \\ \pm i \end{pmatrix}$, the output light becomes

$$E_{out} = \frac{r_{xx} + r_{yy}}{2} \begin{pmatrix} 1 \\ \pm i \end{pmatrix} + \frac{r_{xx} - r_{yy}}{2} \exp(\pm i2\theta) \begin{pmatrix} 1 \\ \mp i \end{pmatrix} \tag{3}$$

where the first term represents the co-polarized CP light while the second term describes the cross-polarized CP wave that gains an additional geometric or Pancharatnam-Berry (PB) phase shift of $\pm 2\theta$ related to the rotation of the meta-atom [38–40]. Particularly, a 2π phase coverage can be achieved by rotating an identical meta-atom from 0° to 180° with a fine step as small as possible. Additionally, the efficiency of geometric phase metasurfaces can be boosted by designing efficient meta-HWPs satisfying the condition of $r_{xx}+r_{yy} = 0$. In this sense, the geometric phase itself is dispersionless because the phase modulation of the cross-polarized CP light is solely determined by the orientation of a single meta-atom. However, it should be noted that the cross-polarized efficiency of the CP light is still typically limited by the dispersion of the meta-atom. Nevertheless, the orientation-induced geometric phase from just one identical meta-atom is more broadband, superior to the resonance phase contributed from several meta-atoms with different dimensions and spectral responses. In Equation (3), the geometric phase is spin locked, which shows opposite signs for the right circularly polarized (RCP) and left circularly polarized (LCP) waves. To release this limitation, multiple HWP with intrinsic resonant phase φ_{xx} should be adopted to modulate the output wave [40]:

$$E_{out} = |r_{xx}|\, e^{i\varphi_{xx}} \exp(\pm i2\theta) \begin{pmatrix} 1 \\ \mp i \end{pmatrix} \tag{4}$$

where the RCP and LCP output waves gain the different phase shifts of $\varphi_{xx} \pm 2\theta$ under the LCP and RCP excitations, respectively.

3. STATIC MULTIFUNCTIONAL GSP METASURFACES

After introducing the fundamentals of GSP metasurfaces, we will first discuss our efforts in exploring the fascinating applications of static multifunctional metasurfaces, including beam-steerers, SPP couplers, metalenses, and meta-waveplates.

3.1. GSP Metasurfaces for Beam-Steering

In 2011, Capasso's group has conceptionally proposed the generalized Snell's law of reflection and refraction for an ultrathin interface with phase discontinuity between two ordinary media by designing an artificial phase gradient metasurface [7]. Considering an incident plane wave impinging at an angle of θ_i on the interface with a local phase gradient of $\frac{\partial \emptyset_x}{\partial x}$, the generalized laws of reflection can be written as:

$$n_i \sin\theta_r - n_i \sin\theta_i = \frac{\lambda_0}{2\pi}\frac{\partial \emptyset_x}{\partial x} \tag{5}$$

where n_i is the refractive index of the medium, θ_r the reflected angle, and λ_0 the free-space wavelength. In this case, the propagating light would be reflected in an anomalous direction, which can be controlled by the designed gradient metasurfaces and thus used for arbitrary beam-steering. To realize a metasurface with a phase discontinuity, Capasso's group has designed anisotropic V-shaped Au meta-atoms to provide abrupt and position-dependent phase shifts for the cross-polarized light at the middle infrared range. Soon after, a similar design has been extended to the near-infrared range with the broadband beam-steering capability [41]. However, V-shaped nanoantennas only allow one to achieve the 2π phase coverage for the transmitted/reflected light polarized orthogonally to the incident wave, that is to say, cross-polarized waves. Worse still, the upper bound to the efficiency of this single-layered meta-atom is 25% even though the absorption is negligible [42, 43]. To handle these two issues, one can place the metal nanoantenna close to a metal reflector with a subwavelength thickness to form a GSP metasurface, which supports both electric and magnetic resonances and thus results in complete phase and polarization control of co- and cross-polarized reflected fields with high efficiency up to 100% [13, 16]. Therefore, highly-efficient beam-steering can be accordingly demonstrated for both LP and CP light [23, 24, 44–51]. Early in 2012, Zhou's and Tsai's groups have collaboratively proposed and demonstrated highly-efficient and broadband beam steering in the near-infrared range by using a gradient GSP metasurface (Figure 1(a)) [44]. Based on an Au-MgF_2-Au triple-layered configuration, the fabricated metasurface can steer the incident light to an anomalous reflection beam without any polarization conversion. Impressively, the measured efficiency is found as high as $\sim 80\%$ with the remaining 20% of the incident energy absorbed at $\lambda = 850\,\text{nm}$. In addition, this gradient GSP metasurface can work in a wide wavelength spectrum with the operation bandwidth $> 150\,\text{nm}$. Once the incident angle gets sufficiently large, the reflected angle predicted by the generalized Snell's law is larger than 90° and the reflected wave becomes a bounded surface wave [52]. In addition to steering the reflected beam of just one specific linear polarization, it is more desired to independently manipulate two orthogonally LP beams at the same time [23, 24]. As such, anisotropic GSP meta-atoms possessing distinct optical responses upon two linear polarizations should be properly selected and arranged to form a metasurface supercell, as shown in the top panel of Figure 2(b) [23]. For TM polarization, the meta-atoms comprising the supercell provide an incremental phase step, thereby resulting in a positive linear phase gradient and anomalous reflection into the +1-diffraction order. On the contrary, the TE-polarized light experiences a negative phase gradient along the x-direction and is reflected into the -1-diffraction order. As shown in the bottom panel of Figure 2(b), linear-polarization-splitting has been achieved with strong intensity contrasts between the spots redirected to the ± 1 orders. At the design wavelength of 800 nm, the fabricated sample can direct $\sim 50\%$ of the incident light into the desired diffraction order, which is slightly lower than the simulated value of 80% due to the fabrication imperfections, the additional loss of the adhesion titanium (Ti) layers, and increased loss of the deposited Au film. When gradient GSP metasurfaces come to the visible range, the dimensions should be properly scaled down, resulting in smaller sizes and increased resolution in fabrication. To fix this fabrication constrain, continuous phase shift from single gradient trapezoid-shaped nanorod antenna has been adopted for steering the visible light [45, 46]. Meanwhile, the high-order GSP resonance supported in meta-atoms with larger sizes can be used but at the expense of lower efficiency [50, 51].

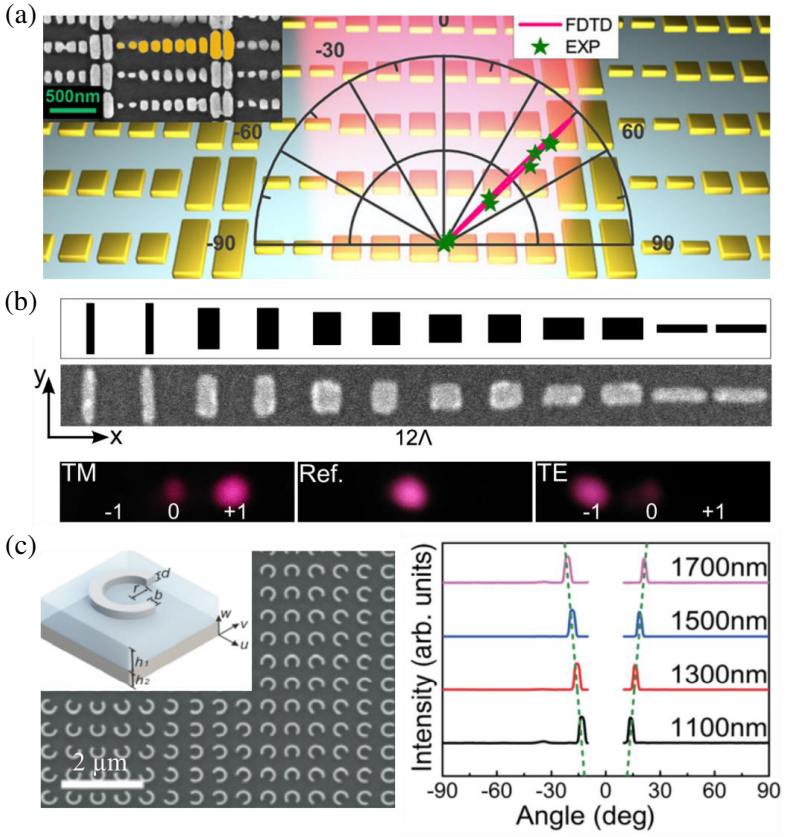

Figure 2. GSP metasurfaces for beam-steering. (a) Schematic and demonstration of high-efficiency beam-steering for near-infrared light by using a gradient GSP metasurface. The inset shows the SEM image of part of the fabricated sample. Reproduced from Ref. [44]. (b) Top panel: schematic and SEM image of the GSP supercell for splittingtwo linear polarizations. Bottom panel: Optical images of the diffraction spots for the metasurface sample and reference sample (Ref.) composed of a 100-nm-thick Au film covered by 50-nm-thick SiO_2 layer at $\lambda = 800\,\text{nm}$. Reproduced from Ref. [23]. (c) Left panel: SEM image of the fabricated GSP metasurface for splitting circular polarizations. The inset shows the metasurface building block consisting of an Ag split ring on top of a SiO_2-Ag substrate. Right panel: angle-resolved intensity distributions at different wavelengths. Reproduced from Ref. [47].

Even though the aforementioned GSP metasurfaces could realize beam-steering in a relatively wide wavelength range, their operation bandwidths are still limited to some extent since the dimension-dependent resonance phase has been utilized. Due to the dissimilar dispersion of all meta-atoms, the bandwidth of the metasurface is intrinsically constrained by the meta-atom with the narrowest bandwidth. Meanwhile, more meta-atoms with different sizes would be really demanding for the fabrication. To overcome this inherent limitation and release the fabrication, geometric phase that enables a full phase control of the cross-polarized CP light by using spatially-varied meta-atoms with uniform dimensions under CP incidence has been widely used [53–57], following the early work on space-variant subwavelength gratings by Hasman and co-workers [38, 39]. Figure 2(c) shows an example of circular-polarization-controlled beam-steering based on the geometric phase metasurface consisting of silver (Ag) split-ring resonators with different rotations, a SiO_2 spacer layer, and a bottom Ag continuous film [47]. In this design, each GSP element functions as a high-performance reflective HWP in the near-infrared range. Under the excitation of an LP beam, the fabricated metasurface can reflect the RCP and LCP components to the ± 1 diffraction orders over a broad wavelength range from 1100 to 1750 nm with the overall diffraction efficiencies approaching $\sim$ 70% (right panel of Figure 2(c)), much higher than those of single-layered geometric metasurfaces [7, 41]. The measured diffraction angle

increases with the increased wavelength, which is in good agreement with the predicted trend from the generalized Snell's law [7]. Due to the conjugated nature of the geometric phase, the RCP and LCP reflected waves are symmetrically distributed with respect to the normal of the interface, which can be broken by using spin-decoupled metasurfaces combining the resonance and geometric phases [40], indicated by Equation (4).

3.2. GSP Metasurfaces for SPP Excitation

From Equation (5), it is clear that there is a critical incident angle of $\theta_c = \sin^{-1}(1 - \frac{1}{n_i}\frac{\lambda_0}{2\pi}\frac{\partial \emptyset_x}{\partial x})$, above which the reflected angle exceeds 90° and the reflected wave becomes a bounded surface wave, such as SPPs in the optical range. On the other hand, the normally incident light will be converted into SPPs if the linear phase gradient provided by the metasurface is matched to the wavevector of SPPs. In 2012, Zhou's group has proposed and demonstrated the first meta-coupler that links the free-propagating wave and the surface wave with $\sim 100\%$ coupling efficiency in the microwave range [52]. Since the driven surface wave is not the eigen mode of the metasurface, an artificial mushroom-type metasurface has been designed to transmit the surface wave. Later on, Bozhevolnyi's group has extended this concept and demonstrated the first unidirectional linear-polarization-controlled SPP excitation by independently and simultaneously manipulating two orthogonal linear polarizations of reflected light with GSP-based gradient metasurfaces in the telecom range [58]. As shown in the left panel of Figure 3(a), the 2D linear-polarization-sensitive SPP meta-coupler consists of 6×6 supercells, in which nine basic GSP meta-atoms with different dimensions are arranged, forming the required linear phase gradients in both x- and y-directions to excite SPPs that propagate in the interface consisting of air, a 50-nm-thick SiO_2 spacer, and an 80-nm-thick Au film. At the design wavelength of 1500 nm, the fabricated meta-coupler can efficiently and selectively excite SPPs with the measured coupling efficiency $\sim 25\%$ and the directionality exceeding 150 (right two panels of Figure 3(a)). Owing to the broadband nature of GSP metasurfaces, this SPP meta-coupler can work properly over a wide spectrum range from 1400 to 1600 nm. Similar to beam-steering, the geometric phase metasurface could be utilized for circular-polarization-controlled unidirectional SPP excitation [59].

In addition to the single functionality of beam-steering or SPP launching in the desired direction, it is more interesting and important to integrate these two functionalities and realize polarization-controlled bifunctional optical meta-devices. As a good example, Figure 3(b) shows a visible bifunctional GSP-based gradient metasurface capable of launching unidirectional SPPs and steering reflected beam anomalously under the excitation of x- and y-polarized waves at normal incidence, respectively [60]. In this design, two distinct linear phase gradients (i.e., $\frac{\partial \emptyset_x}{\partial x}$ and $\frac{\partial \emptyset_y}{\partial x}$) are supplied by a GSP supercell consisting of six anisotropic Ag-SiO_2-Ag meta-atoms. Therefore, the metasurface functions as a polarization-sensitive phase grating for the two linear polarizations, with the phase gradient $\frac{\partial \emptyset_x}{\partial x}$ matched to the SPP wavevector while the phase gradient $\frac{\partial \emptyset_y}{\partial x}$ smaller than the wavevector of the propagating wave in free space. Under the x-polarized excitation, unidirectional SPP excitation was observed from 600 to 650 nm with an averaged coupling efficiency larger than 25%. When the excitation is switched to y-polarization, the incident light is redirected to +1 diffraction order. Akin to this linear-polarization-controlled SPP meta-coupler, the circular polarizations have also been used to encode the functionalities of SPP unidirectional excitation and beam-steering into a single meta-device, as shown in Figure 3(c) [61]. Meng et al. have designed several spatially-rotated GSP meta-HWPs that possess both resonance and geometric phases to provide two distinct linear phase gradients along the x-axis under two CP waves, thereby enabling SPP excitation and anomalous reflection at the same time. The fabricated spin-controlled bifunctional meta-device enables unidirectional SPP launching and beam-steering in a broadband spectrum ranging from 800 to 950 nm with the averaging efficiencies reaching 22% and 48% for the RCP and LCP normally incident light, respectively.

As a final comment, it should be mentioned that even though GSP-based meta-couplers can work in a wide range of wavelengths and incident angles, the coupling efficiency is quite sensitive to the incident beam size, ascribed to the inter- and intra-supercell scattering.

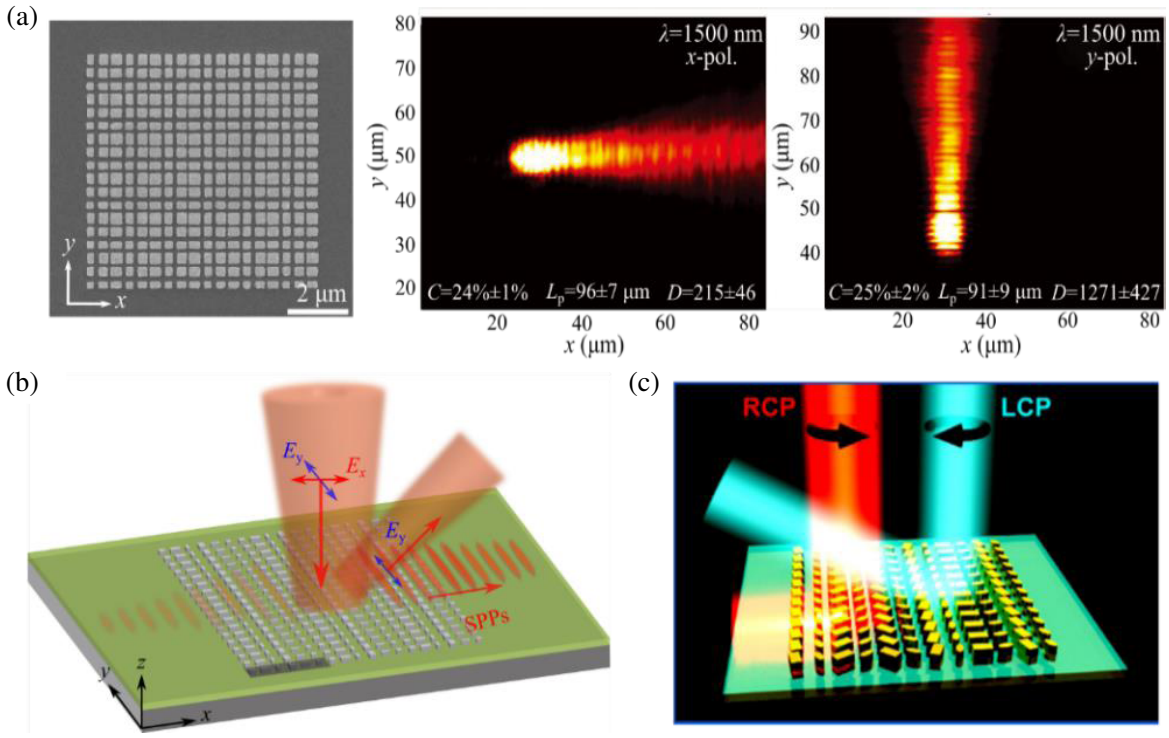

Figure 3. GSP metasurfaces for polarization-controlled SPP excitation. (a) Left panel: SEM image of the fabricated linear-polarization-sensitive SPP meta-coupler composed of 6×6 supercells. Right two panels: recorded leakage radiation microscopy images for two linear polarizations at $\lambda = 1500\,\text{nm}$. Reprinted from Ref. [58]. (b) Schematic of a bifunctional visible GSP metasurface for linear-polarization-controlled SPP excitation and beam-steering at normal incidence. Reprinted from Ref. [60]. (c) Schematic of a bifunctional near-infrared GSP metasurface for spin-controlled SPP excitation and beam-steering at normal incidence. Reprinted from Ref. [61].

3.3. GSP Metalenses

Aside from simple linear phase gradients, GSP metasurfaces can produce arbitrary phase distributions with subwavelength spatial precision, thereby enabling advanced wavefront shaping beyond beam-steering. Among all the potential applications, planar metalenses are especially appealing as they can get rid of the particular surface topography while maintaining comparable or even better focusing performance. In the section, we would like to highlight some typical GST metalenses working in the reflection mode [62–65]. Figure 4(a) shows the first one dimensional (1D) metalens that focuses the x-polarized near-infrared light by imposing the following hyperboloidal phase profile:

$$\phi(x) = \frac{2\pi}{\lambda_0}\left(\sqrt{x^2+f^2} - f\right) \tag{6}$$

where f is the designed focal length [63]. The continuously varying phase profile is first discretized and then represented by eight meta-atoms that provide the approximated phase values, as shown in the left panel of Figure 4(a). Upon the excitation of an x-polarized wave in the wavelength range from 750 to 950 nm, the fabricated $17.3 \times 17.3\,\mu\text{m}^2$ flat metalens demonstrates tight 1D focusing along the x-direction, with the average efficiency ranging between 14% to 27%, considerably smaller than the calculated efficiency of 50% to 78% (right panel of Figure 4(a)). Similar to the linear-polarization beam-steering based on birefringent GSP meta-atoms, polarization-selective focusing can be designed [64]. Figure 4(b) schematically illustrates a multifunctional metalens for simultaneous focusing and linear polarization splitting, where proper anisotropic meta-atoms have been chosen to impose two different hyperboloidal phase profiles to split orthogonal LP polarizations and focus them into two focal spots

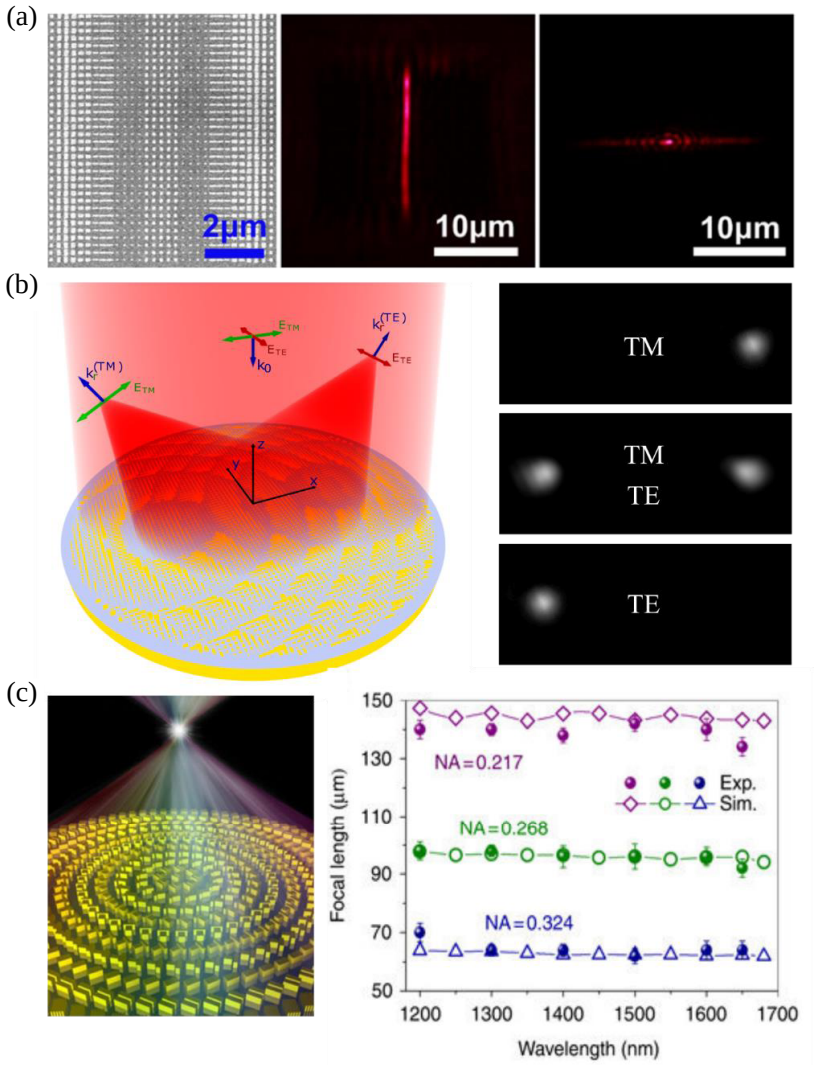

Figure 4. GSP metalenses. (a) Left panel: SEM image of GSP metalens for 1D focusing. Right panel: optical images obtained with the sample placed at different planes at $\lambda = 800\,\text{nm}$. Reprinted from Ref. [63]. (b) Left panel: schematic of a multifunctional metalens for focusing and linear polarization splitting. Right panel: optical images of the focal spots under the excitation of different polarization states at $\lambda = 800\,\text{nm}$. Reprinted from Ref. [64]. (c) Left panel: schematic of an achromatic metalens for focusing broadband near-infrared waves into a single spot. Right panel: simulated and measured focal lengths as a function of the wavelength for the metalenses with different NAs. Reprinted from Ref. [65].

accordingly. As shown in the right panel of Figure 4(b), the fabricated metalens focuses the TM-polarized Gaussian beam to a focal spot on the right side and the TE-polarized Gaussian beam to the left side. When both TM- and TE-polarizations are incident on the metalens, two focal spots are symmetrically generated. The measured efficiency is found to approach 65% in the near-infrared range from 750 to 950 nm. Compared to the conventional polarization beam splitter, this device can boost the polarization extinction ratio up to $\sim 30\,\text{dB}$.

Like conventional lenses that suffer from chromatic aberrations due to the dispersion of the materials, metasurface-enabled lenses have faced the same problem because of the dispersion nature of meta-atoms. Therefore, the corresponding focal length of a metalens is typically inversely proportional to the operating wavelength. Even though this wavelength-dependent focusing can be utilized for certain applications, it is more desirable to achieve achromatic metalenses that work in a continuous wavelength

range. To eliminate chromatic aberrations, Tsai's group has combined the integrated-resonant unit element with smooth and linear phase dispersion and the geometric phase to compensate the phase at different wavelengths for achromatic meta-devices (the left panel of Figure 4(c)) [65]. In particular, they have demonstrated a broadband achromatic flat metalens in the telecom range, which focuses the cross-polarized CP waves at different wavelengths into a diffraction-limited spot under the CP excitation. As shown in the right panel of Figure 4(c), the fabricated metalenses with different numerical apertures (NAs) indicate unchanged focal lengths for varied incident wavelengths spanning from 1200 to 1680 nm. However, the focusing efficiency is rather limited to $\sim 12\%$ since a large number of GSP meta-atoms are employed for phase compensation, which, on the other hand, sacrifices the efficiency.

3.4. Multifunctional GSP Meta-Waveplates

Polarization, the intrinsic property of light that is uncorrected with amplitude, phase, and frequency, is very important for numerous applications, such as material property analysis, biomedical sensing, and information processing [66], since it can provide abundant valuable information. To produce polarized light with a well-defined state of polarization (SoP) from randomly polarized light sources possessing an equal mixture of different polarizations, bulky polarizers and waveplates are required. Typically, optical waveplates are made up of birefringent materials to induce sufficiently large phase retardation between two orthogonally polarized electric fields. Due to the small birefringence of natural materials, the resulting waveplates should be thick enough to accumulate the phase difference, thereby limiting the potential applications in integrated photonics but, in turn, boosting the development of metasurface-based waveplates. Different from bulky optical waveplates with limited birefringence, metasurfaces enable strong and arbitrary birefringence at any wavelength by designing anisotropic meta-atoms with linear-polarization-dependent responses, leading to miniaturized high-performance meta-waveplates with multiple diversified functionalities [67]. Here we discuss multifunctional GSP-based meta-HWPs [68–71] and meta-QWPs [14, 72–75] with the unprecedented capabilities of wavefront shaping beyond the conventional functionality of polarization transformation [31–36].

The first example of multifunctional meta-HWPs is shown in Figure 5(a), where four Au-SiO_2-Au GSP meta-atoms are arranged in a supercell to construct a background-free HWP that combines the functionalities of linear-to-linear polarization conversion and beam-steering in the near-infrared region [68]. Specifically, these four meta-HWPs all enable efficient orthogonal linear-polarization conversion and the complete phase control over cross-polarized reflected fields, thereby forming a universal GSP metasurface platform. By arranging the four meta-atoms in a consequence with an incremental phase step of $\pi/4$, a linear phase gradient along the x-direction is achieved for the cross-polarized reflected fields, resulting in the anomalous reflection in the cross-polarized channel (the left and middle panels of Figure 5(a)). Therefore, the co- and cross-polarized reflected waves can be well-separated in space. In the +1-diffraction order, the cross-polarized reflected wave is dominating while the co-polarized counterpart is completely suppressed (the right panel of Figure 5(a)). As such, the polarization conversion efficiency is greatly enhanced. Quantitatively, the ratio of the integrated power in the cross-polarized channel to the remaining co-polarized power is above 20. Capitalizing on this platform, multifunctional meta-HWPs involving linear-polarization conversion and focusing are experimentally demonstrated to generate various kinds of focused beams with distinct phase distributions and wavefronts, reproducing thereby the combined functionalities of a conventional HWP, a lens, and evena spatial light modulator [69–71]. Figure 5(b) shows a dual-focal metalens that focuses an incident Gaussian beam to two slightly-focused spots with different wavefronts in the cross-polarized channel by segmenting two sub-metalenses [70]. As displayed by the SEM image in Figure 5(b), the fabricated dual-focal metalens consists of two sub-metalenses by imposing different phase profiles with proper meta-atoms that are arranged with a uniform rotation of 45° with respect to the x-axis to ensure the orthogonal linear polarization conversion. Besides the hyperboloidal phase term for focusing, an additional azimuthally-dependent spiral phase profile has been added for focused vortex beam generation. As such, the right metalens shows a spiral pattern while the left metalens has a circular pattern. The right panel of Figure 5(b) shows the intensity distributions at the focal plane, where two tiny focal spots are clearly observed. The diffraction-limited spot on the left has a Gaussian-shaped profile while the focal spot on the right possesses a doughnut shape with zero intensity in the center regardless of the linear polarizer in front of the CCD camera, indicating the excellent phase realization. If

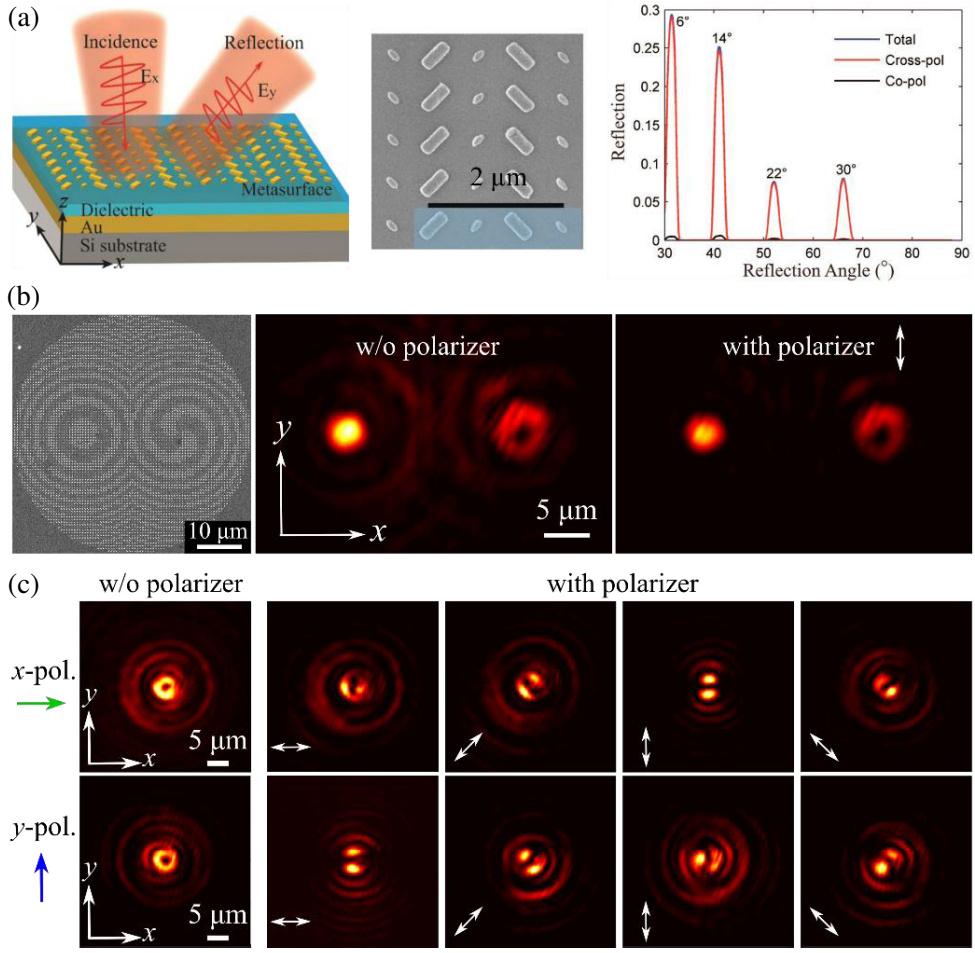

Figure 5. Multifunctional GSP meta-HWPs. (a) Left panel: schematic of the background-free GSP meta-HWP with four meta-atoms as a supercell that enables linear polarization conversion and anomalous reflection in the cross-polarized channel. Middle panel: SEM image of part of the fabricated sample. Right panel: measured reflection with different polarization filters as a function of incident angle for x-polarization at $\lambda = 1000\,\text{nm}$. Reprinted from Ref. [68]. (b) Left panel: SEM image of part of the fabricated dual-focal metalens that creates a convention focused Gaussian beam and a focused vortex beam in the cross-polarized channel. Middle and right panels: measured intensity profiles at the corresponding focal planes without (middle) and with (right) polarization analyzer at $\lambda = 850\,\text{nm}$ under the excitation of an x-polarized Gaussian beam. Reprinted from Ref. [70]. (c) Measured intensity profiles of the meta-HWP lens sample at the corresponding focal planes in the x-y plane with and without a linear polarizer at $\lambda = 850\,\text{nm}$ for x- and y-polarized incident light, respectively. Reprinted from Ref. [71].

a linear polarizer was inserted into the setup to filter out the remaining co-polarized light, the intensity profiles remain largely unaffected and the moderate background is completely removed, qualifiedly manifesting the high-performance of our metasurface for orthogonal linear polarization conversion.

The polarization properties of the demonstrated multifunctional GSP meta-HWPs can be designed on demand, beyond the aforementioned homogeneous polarization distribution. In particular, vector-beams, characterized by a spatially varied distribution of polarization vector, have opened new degrees of freedom for numerous unique functionalities and potential applications in nanophotonics [76, 77]. Our group has implemented the meta-atoms to realize a multifunctional meta-HWP lens for vector-beam generation and focusing [71], distinct from conventional schemes requiring lenses and other bulky optical components. Under the excitation of an x- or y-polarized Gaussian beam, slightly focused

radially-polarized (RP) or azimuthally-polarized (AP) vector-beams can be generated. In our design, the meta-atoms with different sizes and corresponding phase values are first selected and arranged by undergoing a hyperbolic phase distribution. Then they are spatially rotated with the angle of $\varphi/2$–$\pi/2$, where $\varphi = \arctan(y/x)$ is the azimuthal angle in the local position. In this way, the reflected secondary waves possessing spatially-distributed linear polarizations constructively interference at the focal plane to produce focused vector beams. When the incident light is x-polarized, the focused doughnut-shaped spot splits into two side lobes aligned along with the orientation of the polarizer, revealing the focused RP beam generation (top panel of Figure 5(c)). If the incident light is changed to y-polarization, the two side lobes remain perpendicular to the polarization axis, thereby producing a focused AP beam (bottom panel of Figure 5(c)).

Similar to multifunctional meta-HWPs, advanced wavefront shaping capabilities could be realized by spatially integrating multiple QWP meta-atoms to supply versatile phase modulation. Here we take the structured light generation [37, 72, 73] and beam-steering [14, 74] as examples to show the capabilities of multifunctional meta-QWPs under CP excitations. Figure 6(a) shows a vector vortex beam (VVB) generator by utilizing spatially-oriented QWP meta-atoms with $\sim 85\%$ circular-to-linear polarization conversion efficiency [37]. Under the excitation of an RCP wave, the reflected beam has an inhomogeneous LP distribution with the angle of linear polarization (AoLP) equal to the azimuthal angle, generating an RP beam. Additionally, this RP beam has a spiral phase term with the topological charge of $l = -1$. For the LCP excitation, an AP beam carrying a topological charge of $l = 1$ is produced. In the investigated wavelength range from 750 to 950 nm, the fabricated VVB generator could produce RP and AP beams carrying orbital angular momentum with the measured efficiencies of 72% and 68% for RCP and LCP excitations. Freshly, Zhou's group has utilized several QWP meta-atoms with different phase responses to generate arbitrary vector optical fields [73].

Regarding the meta-QWPs for beam-steering, a typical example is shown in Figure 6(b), where simultaneous circular-to-linear polarization conversion and power splitting have been realized by a meta-QWP supercell composed of two different elements with high circular-to-linear polarization conversion efficiencies and a relative phase difference of π between the reflected LP beams [74]. The fabricated meta-QWP shows excellent performance of power splitting, with the incident power equally redirected to the ± 1 diffraction orders and other orders completely suppressed, as shown in the right panel of Figure 6(b). Meanwhile, the split two beams have well-defined linear-polarization states. If the number of designed QWP elements is increased, the functionalities can be extended. For instance, by integrating four high-performance QWP meta-atoms with different resonances phases in a supercell, unidirectional beam-steering along with circular-to-linear polarization conversion has been demonstrated under the CP excitation very recently [14]. More importantly, two spatially separated LP beams with different AoLPs have been simultaneously generated in the opposite directions (left panel of Figure 6(c)) by interweaving two metasurface sub-supercells, where QWP meta-atoms are rotated by 45° or 135° along the counterclockwise direction in the first and second rows, respectively. Upon the RCP excitation, the fabricated metasurface could steer the reflected x- and y-polarized waves into -1 and $+1$ diffraction orders with the measured degrees of linear polarization of $\sim 99.36\%$ and $\sim 99.54\%$, respectively (right panel of Figure 6(c)).

4. DYNAMIC MULTIFUNCTIONAL GSP METASURFACES

Despite significant advances, most reported GSP metasurfaces are static and feature well-defined optical functionalities determined by metasurface configurations that are fixed after fabrication, thereby hindering their implementations in intelligent and adaptive photonic systems where externally controlled reconfigurable responses are required [78–80]. Generally, the realization of dynamic optical GSP metasurfaces is a rather complicated and arduous issue since the comprising meta-atoms are subwavelength in three dimensions (typically < 500 nm). To realize dynamic GSP metasurface, one of the common approaches relies on incorporating active materials, such as liquid crystals [81, 82], phase change materials [83–87], and others [88–92], whose optical responses can be adjusted by applying external stimuli. However, due to the limited metasurface thickness that corresponds to a short interaction length and tunability of optical constants, the aforementioned dynamic GSP metasurfaces have some unresolved issues, such as slow responses [81, 82], relatively low modulation efficiencies [83, 90],

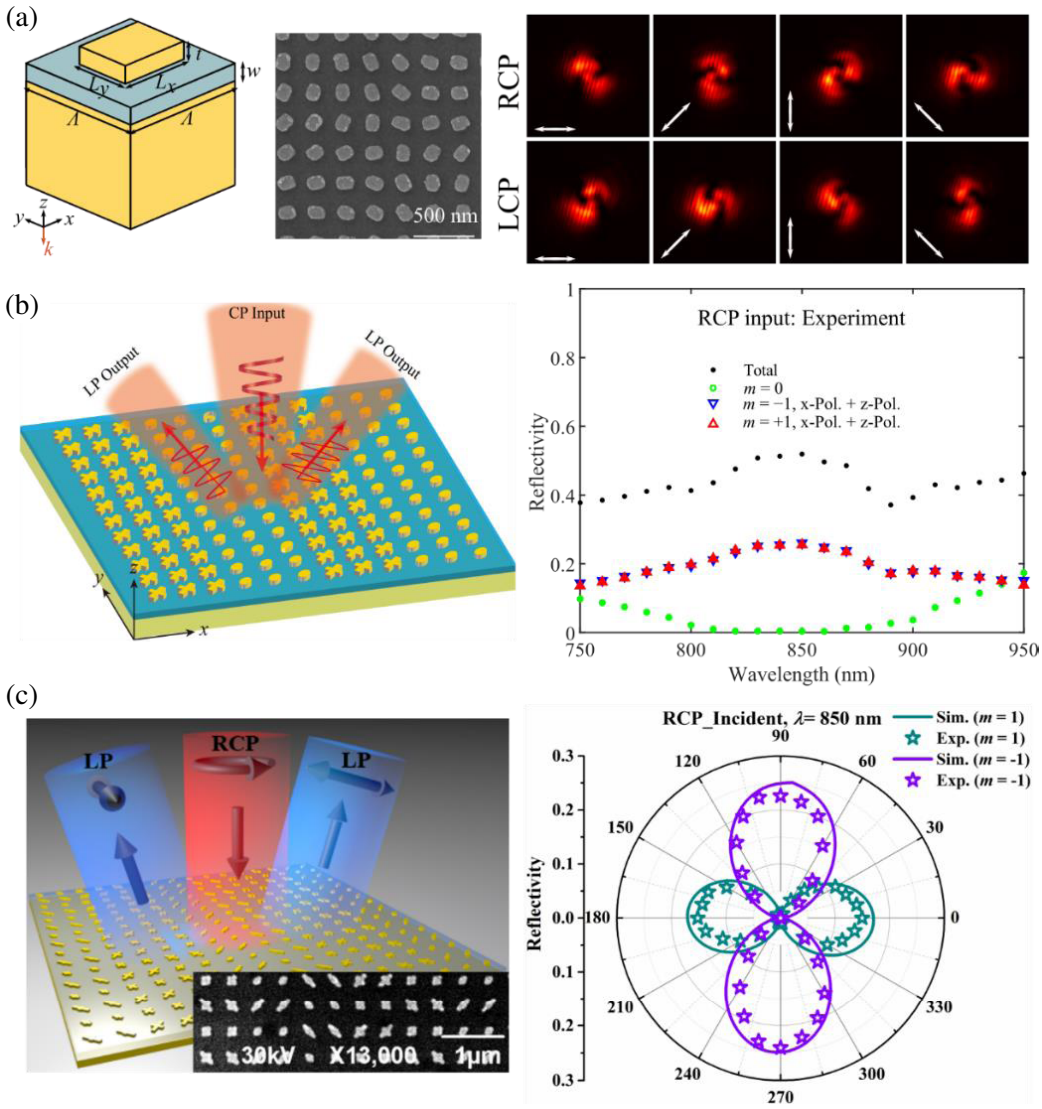

Figure 6. Multifunctional GSP meta-QWPs. (a) Left panel: schematic of the GSP meta-QWP element. Middle panel: SEM image of part of the fabricated sample for VVB generation. Right panel: measured far-field intensity distributions with a linear polarizer under RCP and LCP excitations at $\lambda = 850\,\text{nm}$. Reprinted from Ref. [37]. (b) Left panel: illustration of the GSP meta-QWP for circular-to-linear polarization conversion and power splitting. Right panel: measured diffraction efficiencies as a function of the wavelength under RCP excitation. Reprinted from Ref. [74]. (c) Left panel: illustration of the GSP meta-QWP for generating two diffracted LP beams with different AoLPs under RCP excitation. The inset shows the SEM image of part of the fabricated sample. Right panel: simulated (solid line) and experimental (star markers) polarization state diagrams of the steered beams within ± 1 diffraction orders for RCP excitation at $\lambda = 850\,\text{nm}$. Reprinted from Ref. [14].

and narrow bandwidths [90, 92].

To overcome these drawbacks, we have demonstrated an electrically-driven dynamic GSP metasurface platform by integrating a plasmonic metasurface with a thin-film piezoelectric micro-electro-mechanical system (MEMS) to form a GSP (FP) cavity with a voltage-controlled air gap, which enables dynamic 2D wavefront shaping with high modulation efficiencies, broadband operation, and fast speed by actuating the gap with a proper voltage (Figure 7(a)) [93]. Specifically, by changing the air gap between the plasmonic metasurface layer and MEMS mirror, the response of the overall components

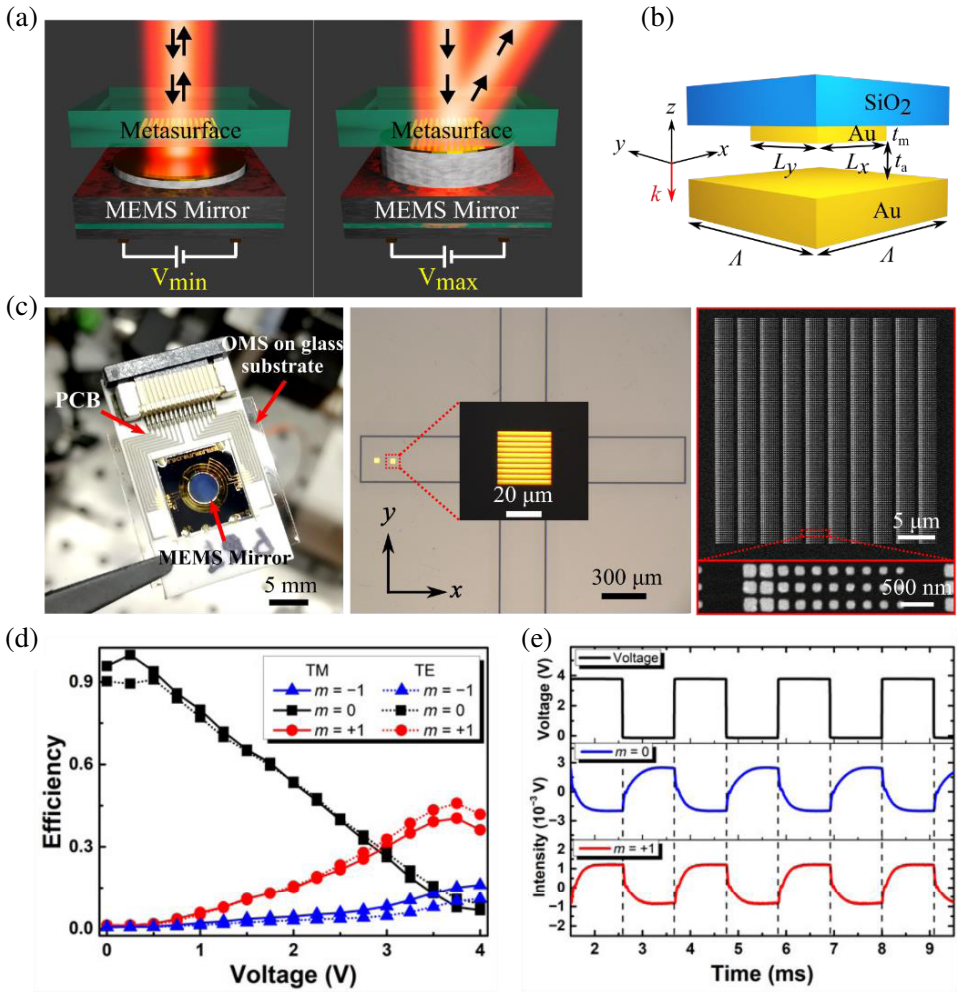

Figure 7. MEMS-integrated dynamic GSP metasurface. (a) Schematic of the dynamic MEMS-metasurface that switches between a reflective mirror and an anomalous beam steerer by applying an actuation voltage. (b) Schematic of the unit cell including the air gap and Au mirror. (c) Typical photo, optical microscope image, and SEM image of the MEMS-metasurface assembly consisting of the Au meta-atoms on a glass substrate, a thin-film MEMS mirror, and a printed circuit board (PCB) for electrical connection. (d) Measured diffraction efficiencies as a function of the voltage for TM/TE incident light at $\lambda = 800\,\text{nm}$. (e) Measure response time for different diffraction orders by actuating the MEMS mirror with a periodic rectangle signal. Reprinted from Ref. [93].

could be redefined in a controllable and reliable way with high precision and resolution. For instance, the dynamic MEMS-metasurface can switch between a reflective mirror and an anomalous beam steerer by applying an actuation voltage (Figure 7(a)). As shown in Figure 7(b), the meta-atom unit cell represents a typical MIM structure consisting of a MEMS mirror, an air gap as the middle spacer, and a top Au brick. At a small air gap of $t_a = 20\,\text{nm}$, the optical responses of meta-atoms are determined by the GSP resonance, with a phase coverage of $\sim 270^\circ$ achieved by varying nanobrick side lengths at the design wavelength of 800 nm. When the air gap is increased, the phase coverage progressively decreases, with the reflection phase and amplitude becoming independent on the nanobrick length at an air gap of $t_a = 350\,\text{nm}$, corresponding to the operation of a convention reflective mirror with the GSP resonance eliminated. In this way, polarization-insensitive dynamic beam steering can be achieved by arranging a number of meta-atoms with different sizes and reflection phases in an array, which forms a linear phase gradient for a given small gap of 20 nm while possessing no phase gradient at a large air gap of 350 nm (Figure 7(c)). The fabricated MEMS-metasurface device exhibits polarization-independent dynamic

beam steering with the reflected power redistributed between the 0th and +1st diffraction orders by increasing the activation voltage from 0 to 3.75 V. In particular, the power between the 0th and +1st diffraction orders reaches the maximum contrast at 3.75 V with the diffraction efficiencies of 40%/46% for the respective TM/TE polarizations, as shown in Figure 7(d). Similar to static GSP metasurfaces, the MEMS-metasurface can operate in a broadband spectrum range near its design wavelength of 800 nm, with a 1 dB bandwidth of $\sim$ 150 nm. In addition to the high efficiency and broadband operation, the device has a fast response with a measured response time shorter than 0.4 ms (Figure 7(e)). As a final comment, we would like to emphasize that the optical metasurface and the MEMS mirror are first fabricated in separate processes and then combined, ensuring thereby the design freedom, and reducing the fabrication complexity. In the near future, we envision more advanced functionalities, such as continuously varied birefringence, switchable OAMs with different topological charges, based on this versatile MEMS-metasurface platform.

5. CONCLUSION AND OUTLOOK

In this mini-review, we have summarized our progress in multifunctional optical GSP metasurfaces, which covers both working principles and emerging applications. Compared to the all-dielectric metasurfaces, the GSP metasurfaces feature reduced device thickness and enhanced operation bandwidths for molding reflected fields with high efficiencies, which are natural for integration with electrical circuits [94]. However, the intrinsic Ohmic loss cannot be completely eliminated. Therefore, near-unity efficiencies can only be achieved with all-dielectric metasurfaces [95]. Meanwhile, the coupling between neighboring GSP meta-atoms is usually significant and should be considered in the design [96], which is different from that in the all-dielectric counterparts that function as individual scatters locally. Due to the unprecedented capabilities of manipulating reflected fields with broadband bandwidths, high efficiencies, high spatial resolutions, compact footprints, and multiple diversified functionalities, optical GSP metasurfaces have been rapidly developing for numerous advanced applications. Here we would like to share our perspectives on two promising directions in the future:

(1) Electrically-driven programmable GSP metasurfaces with independent phase and amplitude control. Despite the significant progress in electrically-driven tunable GSP metasurfaces [81–83, 90, 92–94], there are still unresolved critical issues, restricting severely the applications for adaptive and smart systems. For example, the electrically-driven GSP metasurfaces modulate the phase and amplitude in a coupled way, which significantly limits practical applications. Worse still, such configurations lack the capabilities of independently and simultaneously addressing multiple channels composed of one or several meta-atoms each, far from intelligent and adaptive metasystems. Up to now, electrically-driven GSP metasurfaces with independent phase and amplitude control for programmable and active wavefront manipulation at a submicron pixel-level have not been reported, which will become an emerging research area.

(2) Light-emitting GSP metasurfaces. Even though the aforementioned GSP metasurfaces can provide great flexibility and specific optical responses, most of them are separated from the optical sources and require proper irradiation for the designed optical functionalities. As such, light-emitting GSP metasurfaces that combine optical metasurfaces and light emitters (e.g., solid-state quantum emitters) have received intense interest [97–99]. Very recently, our group has demonstrated quantum metasurface based single-photon sources at room temperature with controlled directionality and polarization states by incorporating meta-atoms with solid-state quantum emitters [98, 99]. We expect universal quantum metasurfaces to appear in this subfield. However, lots of fundamental and technical issues should be solved before such devices can be really used to revolutionize modern quantum technologies.

ACKNOWLEDGMENT

The author acknowledges the funding provided by the Villum Fonden (37372) and Independent Research Fund Denmark (grant No. 1134-00010B).

REFERENCES

1. Veselago, V., "The electrodynamics of substances with simultaneously negative values of ε and μ," *Sov. Phys. Usp.*, Vol. 10, 509–514, 1968.
2. Pendry, J. B., A. J. Holden, D. J. Robbins, and W. J. Stewart, "Magnetism from conductors and enhanced nonlinear phenomena," *IEEE Trans. Microw. Theory*, Vol. 47, 2075–2084, 1999.
3. Pendry, J. B., "Negative refraction makes a perfect lens," *Phys. Rev. Lett.*, Vol. 85, 3966–3969, 2000.
4. Smith, D. and N. Kroll, "Negative refractive index in left-handed materials," *Phys. Rev. Lett.*, Vol. 85, 2933–2936, 2000.
5. Shelby, R. A., D. R. Smith, and S. Schultz, "Experimental verification of a negative index of refraction," *Science*, Vol. 292, 77–79, 2001.
6. Cai, W., U. K. Chettiar, A. V. Kildishev, and V. M. Shalaev, "Optical cloaking with metamaterials," *Nat. Photonics*, Vol. 1, 224–227, 2007.
7. Yu, N., P. Genevet, M. A. Kats, F. Aieta, J.-P. Tetienne, F. Capasso, and Z. Gaburro, "Light propagation with phase discontinuities: Generalized laws of reflection and refraction," *Science*, Vol. 334, 333–337, 2011.
8. Kildishev, A. V., A. Boltasseva, and V. M. Shalaev, "Planar photonics with metasurfaces," *Science*, Vol. 339, 1232009, 2013.
9. Yu, N. and F. Capasso, "Flat optics with designer metasurfaces," *Nat. Mater.*, Vol. 13, 139–150, 2014.
10. Chen, H.-T., A. J. Taylor, and N. Yu, "A review of metasurfaces: Physics and applications," *Rep. Prog. Phys.*, Vol. 79, 076401, 2016.
11. Ding, F., A. Pors, and S. I. Bozhevolnyi, "Gradient metasurfaces: A review of fundamentals and applications," *Rep. Prog. Phys.*, Vol. 81, 026401, 2018.
12. Hsiao, H.-H., C. H. Chu, and D. P. Tsai, "Fundamentals and applications of metasurfaces," *Small Methods*, Vol. 1, 1600064, 2017.
13. He, Q., S. Sun, S. Xiao, and L. Zhou, "High-efficiency metasurfaces: Principles, realizations, and applications," *Adv. Opt. Mater.*, Vol. 6, 1800415, 2018.
14. Deng, Y. D., C. Wu, C. Meng, S. I. Bozhevolnyi, and F. Ding, "Functional metasurface quarter-wave plates for simultaneous polarization conversion and beam steering," *ACS Nano*, Vol. 15, 18532–18540, 2021.
15. Bozhevolnyi, S. I., "Effective-index modeling of channel plasmon polaritons," *Opt. Express*, Vol. 14, 9467–9476, 2006.
16. Ding, F., Y. Q. Yang, R. A. Deshpande, and S. I. Bozhevolnyi, "A review of gap-surface plasmon metasurfaces: Fundamentals and applications," *Nanophotonics*, Vol. 7, 1129–1156, 2018.
17. Yuan, H.-K., U. K. Chettiar, W. Cai, A. V. Kildishev, A. Boltasseva, V. P. Drachev, and V. M. Shalaev, "A negative permeability material at red light," *Opt. Express*, Vol. 15, 1076–1083, 2007.
18. Cai, W., U. K. Chettiar, H.-K. Yuan, V. C. de Silva, A. V. Kildishev, V. P. Drachev, and V. M. Shalaev, "Metamagnetics with rainbow colors," *Opt. Express*, Vol. 15, 3333–3341, 2007.
19. Søndergaard, T. and S. I. Bozhevolnyi, "Slow-plasmon resonant nanostructures: Scattering and field enhancements," *Phys. Rev. B*, Vol. 75, 073402, 2007.
20. Søndergaard, T. and S. I. Bozhevolnyi, "Metal nano-strip optical resonators," *Opt. Express*, Vol. 15, 4198–4204, 2007.
21. Søndergaard, T., J. Jung, S. I. Bozhevolnyi, and G. Della Valle, "Theoretical analysis of gold nano-strip gap plasmon resonators," *New J. Phys.*, Vol. 10, 105008, 2008.
22. Nielsen, M. G., D. K. Gramotnev, A. Pors, O. Albrektsen, and S. I. Bozhevolnyi, "Continuous layer gap plasmon resonators," *Opt. Express*, Vol. 19, 19310–19322, 2011.
23. Pors, A., O. Albrektsen, I. P. Radko, and S. I. Bozhevolnyi, "Gap-plasmon-based metasurfaces for total control of reflected light," *Sci. Rep.*, Vol. 3, 2155, 2013.

24. Pors, A. and S. I. Bozhevolnyi, "Plasmonic metasurfaces for efficient phase control in reflection," *Opt. Express*, Vol. 21, 27438–27451, 2013.
25. Fan, S., W. Suh, and J. D. Joannopoulos, "Temporal coupled-mode theory for the Fano resonance in optical resonators," *J. Opt. Soc. Am. A*, Vol. 20, 569, 2003.
26. Wu, C., B. Neuner, G. Shvets, J. John, A. Milder, B. Zollars, and S. Savoy, "Large-area wide-angle spectrally selective plasmonic absorber," *Phys. Rev. B*, Vol. 84, 07512, 2011.
27. Qu, C., S. Ma, J. Hao, M. Qiu, X. Li, S. Xiao, Z. Miao, N. Dai, Q. He, S. Sun, and L. Zhou, "Tailor the functionalities of metasurfaces based on a complete phase diagram," *Phys. Rev. Lett.*, Vol. 115, 235503, 2015.
28. Liu, N., M. Mesch, T. Weiss, M. Hentschel, and H. Giessen, "Infrared perfect absorber and its application as plasmonic sensor," *Nano Lett.*, Vol. 10, 2342–2348, 2010.
29. Hao, J., J. Wang, X. Liu, W. J. Padilla, L. Zhou, and M. Qiu, "High performance optical absorber based on a plasmonic matematerial," *Appl. Phys. Lett.*, Vol. 96, 251104, 2010.
30. Nielsen, M. G., A. Pors, O. Albrektsen, and S. I. Bozhevolnyi, "Efficient absorption of visible radiation by gap plasmon resonators," *Opt. Express*, Vol. 20, 13311–13319, 2012.
31. Hao, J., Q. Ren, Z. An, X. Huang, Z. Chen, M. Qiu, and L. Zhou, "Optical metamaterial for polarization control," *Phys. Rev. A*, Vol. 80, 023807, 2009.
32. Pors, A., M. G. Nielsen, and S. I. Bozhevolnyi, "Broadband plasmonic half-wave plates in reflection," *Opt. Lett.*, Vol. 38, 513–515, 2013.
33. Dai, Y. M., W. Z. Ren, H. B. Cai, H. Y. Ding, N. Pan, and X. P. Wang, "Realizing full visible spectrum metamaterial half-wave plates with patterned metal nanoarray/insulator/metal film structure," *Opt. Express*, Vol. 22, 7465, 2014.
34. Jiang, Z. H., L. Lin, D. Ma, S. Yun, D. H. Werner, Z. W. Liu, and T. S. Mayer, "Broadband and wide field-of-view plasmonic metasurface-enabled waveplates," *Sci. Rep.*, Vol. 4, 7511, 2014.
35. Jiang, S. C., X. Xiong, Y. S. Hu, Y. H. Hu, G. B. Ma, R. W. Peng, C. Sun, and M. Wang, "Controlling the polarization state of light with a dispersion-free metastructure," *Phys. Rev. X*, Vol. 4, 021026, 2014.
36. Pors, A. and S. I. Bozhevolnyi, "Efficient and broadband quarter-wave plates by gap-plasmon resonators," *Opt. Express*, Vol. 21, 2942–2952, 2013.
37. Heiden, J. T., F. Ding, J. Linnet, Y. Q. Yang, J. Beermann, and S. I. Bozhevolnyi, "Gap-surface plasmon metasurfaces for broadband circular-to-linear polarization conversion and vector vortex beam generation," *Adv. Opt. Mater.*, Vol. 7, 1801414, 2019.
38. Bomzon, Z., G. Biener, V. Kleiner, and E. Hasman, "Radially and azimuthally polarized beams generated by space-variant dielectric subwavelength gratings," *Opt. Lett.*, Vol. 27, 285–287, 2002.
39. Bomzon, Z., G. Biener, V. Kleiner, and E. Hasman, "Space-variant Pancharatnam-Berry phase optical elements with computer-generated subwavelength gratings," *Opt. Lett.*, Vol. 27, 1141–1143, 2002.
40. Qiu, Y. C., S. W. Tang, T. Cai, H. X. Xu, and F. Ding, "Fundamentals and applications of spin-decoupled Pancharatnam-Berry metasurfaces," *Front. Optoelectron.*, Vol. 14, 134–147, 2021.
41. Ni, X., N. K. Emani, A. V. Kildishev, A. Boltasseva, and V. M. Shalaev, "Broadband light bending with plasmonic nanoantennas," *Science*, Vol. 335, 427, 2012.
42. Monticone, F., N. M. Estakhri, and A. Alù, "Full control of nanoscale optical transmission with a composite metascreen," *Phys. Rev. Lett.*, Vol. 110, 203903, 2013.
43. Ding, X., F. Monticone, K. Zhang, L. Zhang, D. Gao, S. N. Burokur, A. Lustrac, Q. Wu, C. Qiu, and A. Alù, "Ultrathin Pancharatnam-Berry metasurface with maximal cross-polarization efficiency," *Adv. Mater.*, Vol. 27, 1195–1200, 2015.
44. Sun, S., K. Y. Yang, C. M. Wang, T. K. Juan, W. T. Chen, C. Y. Liao, Q. He, S. Xiao, W. T. Kung, G. Y. Guo, L. Zhou, and D. P. Tsai, "High-efficiency broadband anomalous reflection by gradient metasurfaces," *Nano Lett.*, Vol. 12, 6223–6229, 2012.
45. Farmahini-Farahani, M. and H. Mosallaei, "Birefringent reflectarray metasurface for beam engineering in infrared," *Opt. Lett.*, Vol. 38, 462–464, 2013.

46. Pors, A., M. G. Nielsen, and S. I. Bozhevolnyi, "Plasmonic metagratings for simultaneous determination of Stokes parameters," *Optica*, Vol. 2, 716–723, 2015.
47. Jiang, S.-C., X. Xiong, Y.-S. Hu, S.-W. Jiang, Y.-H. Hu, D.-H. Xu, R.-W. Peng, and M. Wang, "High-efficiency generation of circularly polarized light via symmetry-induced anomalous reflection," *Phys. Rev. B*, Vol. 91, 125421, 2015.
48. Li, Z., E. Palacios, S. Butun, and K. Aydin, "Visible-frequency metasurfaces for broadband anomalous reflection and high-efficiency spectrum splitting," *Nano Lett.*, Vol. 15, 1615–1621, 2015.
49. Gao, S., W. Yue, C. Park, S. Lee, E. Kim, and D. Choi, "Aluminum plasmonic metasurface enabling a wavelength-insensitive phase gradient for linearly polarized visible light," *ACS Photonics*, Vol. 4, 322–328, 2017.
50. Deshpande, R., A. Pors, and S. I. Bozhevolnyi, "Third-order gap plasmon based metasurfaces for visible light," *Opt. Express*, Vol. 25, 12508–12517, 2017.
51. Deshpande, R. A., F. Ding, and S. Bozhevolnyi, "Dual-band metasurfaces using multiple gap-surface plasmon resonances," *ACS Appl. Mater. Interfaces*, Vol. 12, 1250–1256, 2020.
52. Sun, S., Q. He, S. Xiao, Q. Xu, X. Li, and L. Zhou, "Gradient-index meta-surfaces as a bridge linking propagating waves and surface waves," *Nat. Mater.*, Vol. 11, 426–431, 2012.
53. Huang, L. L., X. Z. Chen, H. Mühlenbernd, G. X. Li, B. F. Bai, Q. F. Tan, G. F. Jin, T. Zentgraf, and S. Zhang, "Dispersionless phase discontinuities for controlling light propagation," *Nano Lett.*, Vol. 12, 5750–5755, 2012.
54. Lin, D. M., P. Y. Fan, E. Hasman, and M. L. Brongersma, "Dielectric gradient metasurface optical elements," *Science*, Vol. 345, 298-302, 2014.
55. Khorasaninejad, M. and K. B. Crozier, "Silicon nanofin grating as a miniature chirality-distinguishing beam-splitter," *Nat. Commun.*, Vol. 5, 5386, 2014.
56. Zheng, G. X., H. Mühlenbernd, M. Kenney, G. X. Li, T. Zentgraf, and S. Zhang, "Metasurface holograms reaching 80% efficiency," *Nat. Nanotechnol.*, Vol. 10, 308–312, 2015.
57. Wu, P. C., W. Y. Tsai, W. T. Chen, Y. W. Huang, T. Y. Chen, J. W. Chen, C. Y. Liao, C. H. Chu, G. Sun, and D. P. Tsai, "Versatile polarization generation with an aluminum plasmonic metasurface," *Nano Lett.*, Vol. 17, 445–452, 2017.
58. Pors, A., M. G. Nielsen, T. Bernardin, J. Weeber, and S. I. Bozhevolnyi, "Efficient unidirectional polarization-controlled excitation of surface plasmon polaritons," *Light: Sci. Appl.*, Vol. 3, e197, 2014.
59. Mühlenbernd, H., P. Georgi, N. Pholchai, L. Huang, G. Li, S. Zhang, and T. Zentgraf, "Amplitude- and phase-controlled surface plasmon polariton excitation with metasurfaces," *ACS Photonics*, Vol. 3, 124–129, 2016.
60. Ding, F., R. Deshpande, and S. I. Bozhevolnyi, "Bifunctional gap-plasmon metasurfaces for visible light: Polarization-controlled unidirectional surface plasmon excitation and beam steering at normal incidence," *Light Sci. Appl.*, Vol. 7, 17178, 2018.
61. Meng, C., S. W. Tang, F. Ding, and S. I. Bozhevolnyi, "Optical gap-surface plasmon metasurfaces for spin-controlled surface plasmon excitation and anomalous beam steering," *ACS Photonics*, Vol. 7, 1849–1856, 2020.
62. Li, X., S. Xiao, B. Cai, Q. He, T. J. Cui, and L. Zhou, "Flat metasurfaces to focus electromagnetic waves in reflection geometry," *Opt. Lett.*, Vol. 37, 4940–4942, 2012.
63. Pors, A., M. G. Nielsen, R. L. Eriksen, and S. I. Bozhevolnyi, "Broadband focusing flat mirrors based on plasmonic gradient metasurfaces," *Nano Lett.*, Vol. 13, 829–834, 2013.
64. Boroviks, S., R. A. Deshpande, N. A. Mortensen, and S. I. Bozhevolnyi, "Multifunctional metamirror: Polarization splitting and focusing," *ACS Photonics*, Vol. 5, 1648–1653, 2018.
65. Wang, S., P. C. Wu, V.-C. Su, Y.-C. Lai, C. Hung Chu, J.-W. Chen, S.-H. Lu, J. Chen, B. Xu, C.-H. Kuan, T. Li, S. Zhu, and D. P. Tsai, "Broadband achromatic optical metasurface devices," *Nat. Commun.*, Vol. 8, 187, 2017.
66. Goldstein, D. H., *Polarized Light*, CRC University, 2017.

67. Ding, F., S. W. Tang, and S. I. Bozhevolnyi, "Recent advances in polarization-encoded optical metasurfaces," *Adv. Photonics Res.*, Vol. 2, 2000173, 2021.
68. Ding, F., Z. X. Wang, S. L. He, V. M. Shalaev, and A. V. Kildishev, "Broadband high-efficiency half-wave plate: A supercell-based plasmonic metasurface approach," *ACS Nano*, Vol. 9, 4111–4119, 2015.
69. Ding, F., Y. T. Chen, and S. I. Bozhevolnyi, "Gap-surface plasmon metasurfaces for linear-polarization conversion, focusing, and beam splitting," *Photonics Res.*, Vol. 8, 707–714, 2020.
70. Ding, F., Y. T. Chen, and S. I. Bozhevolnyi, "Focused vortex-beam generation using gap-surface plasmon metasurfaces," *Nanophotonics*, Vol. 9, 371–378, 2020.
71. Ding, F., Y. Chen, Y. Yang, and S. I. Bozhevolnyi, "Multifunctional metamirrors for broadband focused vector-beam generation," *Adv. Opt. Mater.*, Vol. 7, 1900724, 2019.
72. Yue, F. Y., D. D. Wen, J. T. Xin, B. D. Gerardot, J. Li, and X. Z. Chen, "Vector vortex beam generation with a single plasmonic metasurface," *ACS Photonics*, Vol. 3, 1558–1563, 2016.
73. Wang, D. Y., F. F. Liu, T. Liu, S. L. Sun, Q. He, and L. Zhou, "Efficient generation of complex vectorial optical fields with metasurfaces," *Light Sci. Appl.*, Vol. 10, 67, 2021.
74. Ding, F., R. Deshpande, C. Meng, and S. I. Bozhevolnyi, "Metasurface-enabled broadband beam splitters integrated with quarter-wave plate functionality," *Nanoscale*, Vol. 12, 14106–14111, 2020.
75. Dorn, R., S. Quabis, and G. Leuchs, "Sharper focus for a radially polarized beam," *Phys. Rev. Lett.*, Vol. 91, 233901, 2003.
76. Zhan, Q., "Cylindrical vector beams: From mathematical concepts to applications," *Adv. Opt. Photon.*, Vol. 1, 1–57, 2009.
77. Forbes, A., M. de Oliveira, and M. R. Dennis, "Structured light," *Nat. Photonics*, Vol. 15, 253–262, 2021.
78. Liu, F., O. Tsilipakos, A. Pitilakis, A. C. Tasolamprou, M. S. Mirmoosa, N. V. Kantartzis, D.-H. Kwon, J. Georgiou, K. Kossifos, M. A. Antoniades, M. Kafesaki, C. M. Soukoulis, and S. A. Tretyakov, "Intelligent metasurfaces with continuously tunable local surface impedance for multiple reconfigurable functions," *Phys. Rev. Appl.*, Vol. 11, 044024, 2019.
79. Tsilipakos, O., A. C. Tasolamprou, A. Pitilakis, F. Liu, X. Wang, M. S. Mirmoosa, D. C. Tzarouchis, S. Abadal, H. Taghvaee, C. Liaskos, A. Tsioliaridou, J. Georgiou, A. Cabellos-Aparicio, E. Alarcón, S. Io-annidis, A. Pitsillides, I. F. Akyildiz, N. V. Kantartzis, E. N. Economou, C. M. Soukoulis, M. Kafesaki, and S. Tretyakov, "Towards intelligent metasurfaces: The progress from globally tunable metasurfaces to softwaredefined metasurfaces with an embedded network of controllers," *Adv. Opt. Mater.*, Vol. 8, 2000783, 2020.
80. Pitilakis, A., O. Tsilipakos, F. Liu, K. M. Kossifos, A. C. Tasolamprou, D.-H. Kwon, M. S. Mirmoosa, D. Manessis, N. V. Kantartzis, C. Liaskos, M. A. Antoniades, J. Georgiou, C. M. Soukoulis, M. Kafesaki, and S. A. Tretyakov, "A multi-functional reconfigurable metasurface: Electromagnetic design accounting for fabrication aspects," *IEEE Trans. Antennas Propag.*, Vol. 69, 1440–1454, 2021.
81. Li, J., P. Yu, S. Zhang, and N. Liu, "Electrically-controlled digital metasurface device for light projection displays," *Nat. Commun.*, Vol. 11, 3574, 2020.
82. Yu, P., J. X. Li, and N. Liu, "Electrically tunable optical metasurfaces for dynamic polarization conversion," *Nano Lett.*, Vol. 21, 6690–6695, 2021.
83. Chu, C. H., M. L. Tseng, J. Chen, P. C. Wu, Y. H. Chen, H. C. Wang, T. Y. Chen, W. T. Hsieh, H. J. Wu, G. Sun, and D. P. Tsai, "Active dielectric metasurface based on phase-change medium," *Laser Photonics Rev.*, Vol. 10, 986–994, 2016.
84. De Galarreta, C. R., A. M. Alexeev, Y.-Y. Au, M. Lopez-Garcia, M. Klemm, M. Cryan, J. Bertolotti, and C. D. Wright, "Nonvolatile reconfigurable phase-change metadevices for beam steering in the near infrared," *Adv. Funct. Mater.*, Vol. 28, 1704993, 2018.
85. Ding, F., Y. Yang, and S. I. Bozhevolnyi, "Dynamic metasurfaces using phase-change chalcogenides," *Adv. Opt. Mater.*, Vol. 7, 1801709, 2019.

86. Park, J., S. J. Kim, P. Landreman, and M. L. Brongersma, "An over-coupled phase-change metasurface for efficient reflection phase modulation," *Adv. Opt. Mater.*, Vol. 8, 2000745, 2020.
87. Zhang, Y., C. Fowler, J. Liang, B. Azhar, M. Y. Shalaginov, S. Deckoff-Jones, S. An, J. B. Chou, C. M. Roberts, V. Liberman, M. Kang, C. Rios, K. A. Richardson, C. Rivero-Baleine, T. Gu, H. Zhang, and J. Hu, "Electrically reconfigurable non-volatile metasurface using low-loss optical phase-change material," *Nat. Nanotechnol.*, Vol. 16, 661–666, 2021.
88. Li, Z., K. Yao, F. Xia, S. Shen, J. Tian, and Y. Liu, "Graphene plasmonic metasurfaces to steer infrared light," *Sci. Rep.*, Vol. 5, 12423, 2015.
89. Zeng, B., Z. Huang, A. Singh, Y. Yao, A. K. Azad, A. D. Mohite, A. J. Taylor, D. R. Smith, and H. T. Chen, "Hybrid graphene metasurfaces for high-speed mid-infrared light modulation and single-pixel imaging," *Light Sci. Appl.*, Vol. 7, 51, 2018.
90. Wu, P. C., R. A. Pala, G. KafaieShirmanesh, W. H. Cheng, R. Sokhoyan, M. Grajower, M. Z. Alam, D. Lee, and H. A. Atwater, "Dynamic beam steering with all-dielectric electro-optic III–V multiple-quantum-well metasurfaces," *Nat. Commun.*, Vol. 10, 3654, 2019.
91. Neubrech, F., X. Duan, and N. Liu, "Dynamic plasmonic color generation enabled by functional materials," *Sci. Adv.*, Vol. 6, eabc2709, 2020.
92. Park, J., B. G. Jeong, S. I. Kim, D. Lee, J. Kim, C. Shin, C. B. Lee, T. Otsuka, J. Kyoung, S. Kim, K. Y. Yang, Y. Y. Park, J. Lee, I. Hwang, J. Jang, S. H. Song, M. L. Brongersma, K. Ha, S. W. Hwang, H. Choo, and B. L. Choi, "All-solid-state spatial light modulator with independent phase and amplitude control for three-dimensional LiDAR applications," *Nat. Nanotechnol.*, Vol. 16, 69–76, 2021.
93. Meng, C., P. C. V. Thrane, F. Ding, J. Gjessing, M. Thomaschewski, C. Wu, C. Dirdal, and S. I. Bozhevolnyi, "Dynamic piezoelectric MEMS-based optical metasurfaces," *Sci. Adv.*, Vol. 7, eabg5639, 2021.
94. Damgaard-Carstensen, C., M. Thomaschewski, F. Ding, and S. Bozhevolnyi, "Electrical tuning of Fresnel lens in reflection," *ACS Photonics*, Vol. 8, 1576, 2021.
95. He, T., T. Liu, S. Xiao, Z. Wei, Z. Wang, L, Zhou, and X. Cheng, "Perfect anomalous reflectors at optical frequencies," *Sci. Adv.*, Vol. 8, eabk3381, 2022.
96. Deshpande, R., V. A. Zenin, F. Ding, N. A. Mortensen, and S. I. Bozhevolnyi, "Direct characterization of near-field coupling in gap plasmon-based metasurfaces," *Nano Lett.*, Vol. 18, 6265–6270, 2018.
97. Solntsev, A. S., G. S. Agarwal, and Y. S. Kivshar, "Metasurfaces for quantum photonics," *Nat. Photonics*, Vol. 15, 327–336, 2021.
98. Kan, Y. H., S. K. H. Andersen, F. Ding, S. Kumar, C. Y. Zhao, and S. I. Bozhevolnyi, "Metasurface-enabled generation of circularly polarized single photons," *Adv. Mater.*, Vol. 32, 1907832, 2020.
99. Wu, C., S. Kumar, Y. H. Kan, D. Komisar, Z. M. Wang, S. I. Bozhevolnyi, and F. Ding, "Room-temperature on-chip orbital angular momentum single-photon sources," *Sci. Adv.*, Vol. 8, eabk3075, 2022.